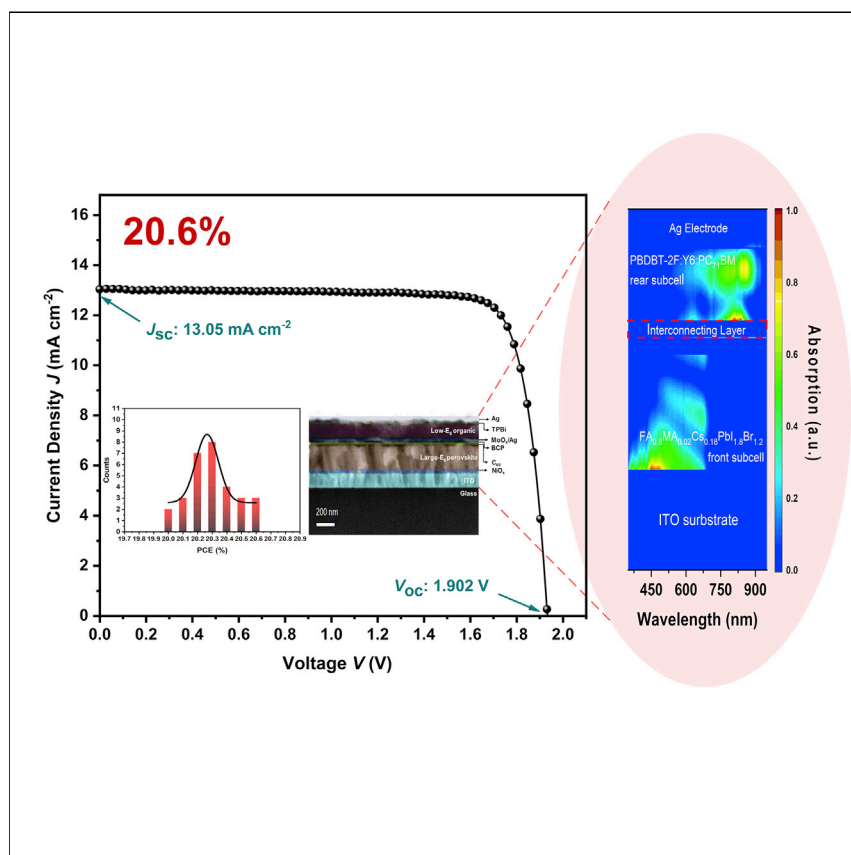


Article

# Efficient and Reproducible Monolithic Perovskite/Organic Tandem Solar Cells with Low-Loss Interconnecting Layers



Xu Chen, Ziyang Jia, Zeng Chen, ..., Wei E.I. Sha, Haiming Zhu, Yang (Michael) Yang

yangyang15@zju.edu.cn

HIGHLIGHTS

A semi-empirical model to select the best available material combination

Orthogonal processing solvents enabling high reproducibility

All-thermally evaporated low-loss interconnecting layers

20.6% efficiency for the champion tandem device (certified as 19.54%)

In this work, we developed a semi-empirical model to calculate the practical PCE limits of perovskite/organic TSCs, instructing us to select the material combinations quickly. Based on it, we selected 1.77 eV perovskite and 1.41 eV organic as two subcells and developed the all-thermally evaporated low-loss interconnecting layers, which ultimately lead to reproducible and efficient TSCs, with PCEs narrowly distributed between 20.0% and 20.6%.

Chen et al., *Joule* 4, 1594–1606  
 July 15, 2020 © 2020 Elsevier Inc.  
<https://doi.org/10.1016/j.joule.2020.06.006>



## Article

# Efficient and Reproducible Monolithic Perovskite/Organic Tandem Solar Cells with Low-Loss Interconnecting Layers

Xu Chen,<sup>1</sup> Ziyang Jia,<sup>1</sup> Zeng Chen,<sup>2</sup> Tingming Jiang,<sup>1</sup> Lizhong Bai,<sup>1</sup> Feng Tao,<sup>1</sup> Jianwu Chen,<sup>1</sup> Xinya Chen,<sup>1</sup> Tianyu Liu,<sup>1</sup> Xuehui Xu,<sup>1</sup> Chenying Yang,<sup>1</sup> Weidong Shen,<sup>1</sup> Wei E.I. Sha,<sup>3</sup> Haiming Zhu,<sup>2</sup> and Yang (Michael) Yang<sup>1,4,\*</sup>

## SUMMARY

Perovskite solar cells (PSCs) and organic photovoltaics (OPVs) have both undergone rapid development recently. The composition and molecular tunability of perovskite and organic semiconductors enable a large material pool with different band gaps and various physical characters, giving feasibility to construct perovskite/organic tandem solar cells (TSCs). Here, we developed a semi-empirical model, rationally selected the best available material combination, and successfully demonstrated the efficient and reproducible TSCs benefiting from their complementary band gaps and orthogonal processing solvents. Featuring with all-thermally evaporated low-loss interconnecting layers (ICLs), our 2-terminal (2T) monolithic perovskite/organic TSCs deliver high reproducibility with power conversion efficiency (PCE) narrowly distributed between 20% and 20.6% (certified as 19.54%). In addition to the promising efficiency, the UV sensitivity of OPVs is eliminated in the tandem structure, demonstrating its advantage on device stability. Those results unfold significant potentials of perovskite/organic tandem devices as reproducible and cost-effective structures to achieve high-performance TSCs.

## INTRODUCTION

It is well known that perovskite solar cells (PSCs) and organic photovoltaics (OPVs) have many common advantages, such as low cost, simple preparation process, and the ability to prepare translucent photovoltaic devices, which have been receiving great attentions over the years.<sup>1,2</sup> The all-perovskite or all-organic tandem solar cell (TSC) is considered as an effective way to overcome the thermalization loss and surpass the Shockley-Queisser (SQ) limit.<sup>3</sup> All-perovskite 2T tandem cells have gradually developed from 17.0% power conversion efficiency (PCE) to 24.8% in the last few years,<sup>4–10</sup> and all-organic 2T tandem cells have reached 17.3% PCE recently.<sup>11–16</sup> However, they need the solvents of similar polarities to process the front and back cells, which elevates the barrier to realize high-performance tandems reproducibly.<sup>17</sup> To fabricate perovskite tandem photovoltaics, it normally requires thick, compact, and high-quality interconnecting layers (ICLs) to protect the front cells by sputtering thick Indium-tin-oxide (ITO) layers or atomically depositing compact TiO<sub>2</sub> (or SnO<sub>2</sub>) layers, which will further increase the fabrication costs, optical losses, and processing difficulties. Thanks to the orthogonal solvents used for dissolving perovskite and organic materials, it is naturally less challenging to

## Context & Scale

Tandem photovoltaic is an effective way to surpass the Shockley-Queisser limit, attracting great attention. In the past few years, the wide-band-gap perovskite solar cells (PSCs) and narrow band-gap organic solar cells (OSCs) have both been growing rapidly, bringing opportunities of making efficient perovskite/organic tandem solar cells (TSCs). Here, we developed a semi-empirical device model to select the best available material combination for perovskite/organic TSCs. Based on it, we selected a wide-band-gap PSC and a ternary OPV and achieved 20.6% PCE featuring with low-loss interconnecting layers. In addition, those TSCs delivered good reproducibility, thanks to the orthogonal solvents used for processing subcells. Furthermore, the photostability of TSCs was enhanced compared with the single-junction OSCs, due to the UV filtering effect of the perovskite layers. Those results inspire bright futures for perovskite/organic TSCs, especially because of the rapid developments of PSCs and OSCs.

construct perovskite/organic tandem cells. In addition, the recent rapid development of low-band-gap organic semiconductors provides various excellent candidates as the back cells,<sup>18,19</sup> whose photovoltaic performances are catching up with the Pb-Sn mixed low-band-gap PSCs.<sup>5,20–24</sup> So far, perovskite/organic tandem structures have been applied in regular, flexible, and semi-transparent solar cells,<sup>25,26</sup> yet the PCEs of previous tandem cells have not shown clear enhancements to the subcells,<sup>27–31</sup> mainly caused by non-ideal band-gap combinations, high loss ICLs, and etc. (Table S1).

Here, we built a semi-empirical device model for perovskite/organic tandem cells. Based on the model, we can estimate the practical PCE limit of different combinations quickly. Considering the current status of PSCs and OPVs, we selected a wide-band-gap perovskite as the front cell and a ternary OPV as the back cell, and achieved monolithic perovskite/organic tandem cell with a PCE of 20.6% (certified 19.54%), reaching a milestone record and demonstrating great potential for this promising device structure.

## RESULTS AND DISCUSSION

### Practical PCE Limit for Perovskite/Organic Tandem Cells

Perovskite-organic tandem strategy is of great potential to surpass the SQ limit of the single-junction cell, without significant increase of processing cost. Before fabricating the tandem device, we first developed a semi-empirical device model to estimate its practical efficiency limit, which guided us toward the best available combination. Compared with other types of solar cells, the luminescent emission shifts of the OPVs, with respect to their band gaps ( $E_g$ ), are much stronger.<sup>18,32</sup> This phenomenon shows that the inevitable voltage loss  $\Delta V_{shift}$  needs to be considered. To make the predicted efficiency closer to reality, we appropriately introduced the non-radiative recombination current ( $J_r$ ) to limit the fill factor ( $FF$ ) of OPVs to be less than 85% (Equation S10), because the  $FF$ s of OPVs can hardly exceed 85% due to their relatively serious non-radiative recombinations.<sup>33–36</sup> Many previous models assumed the full absorption of the above band-gap photons for the front cell. But in reality, the thickness of the perovskite-based front subcell is adjustable, so it is necessary to introduce the term external quantum efficiency (EQE) loss for the front cell ( $EQE_{loss,T}$ ), as a result of the reduced thickness, and it accordingly increased transmittance into the modeling.<sup>11</sup> Those photons, although they have higher energies than perovskite band gap, transmit through the front cell, and then they are utilized by the rear cell. The  $EQE_{loss,T}$  is not an actual loss for the tandem cell, it accounts for a loss of the front cell but a gain of the rear cell. We assumed that  $EQE_{loss,T}$  was no more than 50%,<sup>4–10,28,30,37</sup> and has invariant (noted as *Hypothesis 1*) or linear (noted as *Hypothesis 2*) dependence on the wavelength of the incident light (Equation S15). In our modeling, band gaps of front and rear cells, and  $EQE_{loss,T}$  are all variable parameters that can be optimized to maximize the current density and PCE of the TSCs (Figure S2), while previous models usually consider the mere band-gap values of each subcell.

Figure 1 shows practical PCE limit of perovskite/organic TSCs. Obviously, the perovskite/organic tandems have developed slowly over the past few years, but they also have outstanding potentials: The practical efficiency of the 4T and 2T tandem cells can be over 40% (Figures 1A and 1B), respectively. In recent years, some studies have involved this kind of tandem, but their potentials are not fully realized. The PCEs of the reported devices were below 16%,<sup>25–31</sup> and there remains a true demand to understand and develop such tandem devices.

<sup>1</sup>State Key Laboratory of Modern Optical Instrumentation, College of Optical Science and Engineering, International Research Center for Advanced Photonics, Zhejiang University, Hangzhou, Zhejiang 310058, China

<sup>2</sup>Center for Chemistry of High-Performance & Novel Materials, Department of Chemistry, Zhejiang University, Hangzhou, Zhejiang 310058 China

<sup>3</sup>Key Laboratory of Micro-nano Electronic Devices and Smart Systems of Zhejiang Province, College of Information Science and Electronic Engineering, Zhejiang University, Hangzhou 310027, China

<sup>4</sup>Lead Contact

\*Correspondence: yangyang15@zju.edu.cn  
<https://doi.org/10.1016/j.joule.2020.06.006>

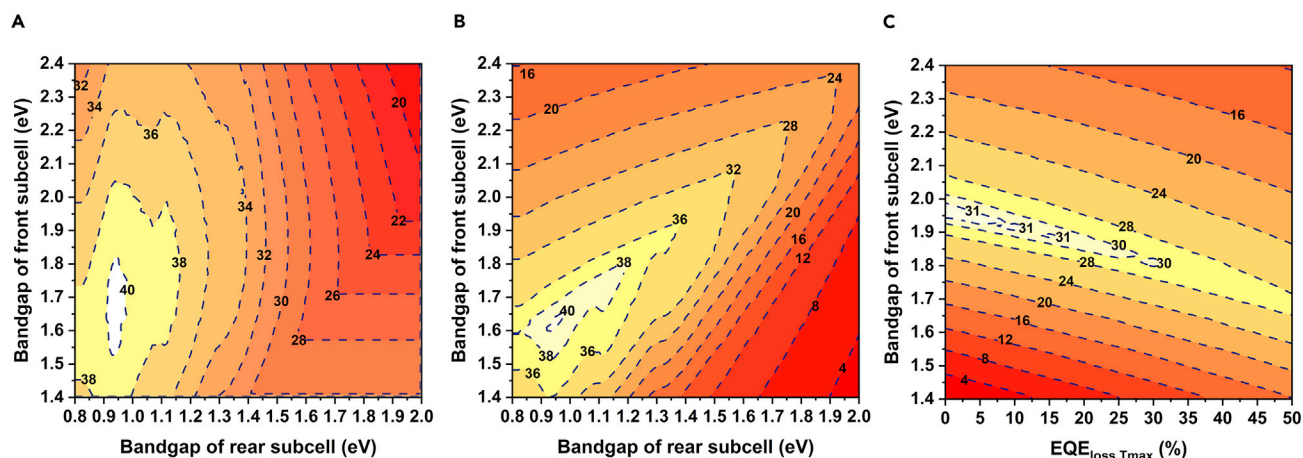


**Figure 1. Practical PCE Limits of Perovskite-Organic Tandem Photovoltaics**

(A and B) Practical efficiency limits of 4T and 2T TSCs; we assume 90% EQE for the front cell and 85% for the rear cell. The unique voltage loss  $\Delta V_{\text{shift}}$  of the organic-based cell is about 0.05 eV,<sup>32</sup> the *FF* is no more than 85%. In the absorption overlap area, the corresponding  $\text{EQE}_{\text{loss,T}}$  for each band-gap combination has been considered.

(C) Practical efficiency limits of Y6-based (1.41 eV) 2T TSCs (Figure S1A), with different front cell band gaps and variable  $\text{EQE}_{\text{loss,Tmax}}$  (0%–50%), the maximum  $\text{EQE}_{\text{loss,T}}$ . For the front cell,  $\text{EQE}_{\text{front}}$  equals 90%– $\text{EQE}_{\text{loss,T}}$  for the overlap regions. For the rear cell, considering its IQE is approaching 100%,<sup>38</sup>  $\text{EQE}_{\text{rear}}$  is equal to  $\text{EQE}_{\text{loss,T}}$  for the absorption overlap area, other than the overlap, the  $\text{EQE}_{\text{rear}}$  is 81% (Equation S12). Hypothesis 2 is applied to calculate the  $\text{EQE}_{\text{loss,T}}$ , expressed by the Equation S15. The  $V_{\text{oc}}$  is 0.845 V and *FF* is 77%, referring to the reported values of Y6-based devices.<sup>39</sup>

First, we applied the semi-empirical model to quantify the potential of OPVs based on different non-fullerenes acceptor (NFA) small molecules as the rear cells. Although absorption onset of the NFA Y6 is not as red as some near infrared (NIR) molecules, such as CO<sub>2</sub>DFT (or named O6T-4F),<sup>40</sup> ITIC-4CI<sup>41</sup> et al., the Y6-based OSCs showed average EQE of nearly 80%, high *FF*, and small open-circuit voltage loss ( $V_{\text{oc}}$ )<sup>19,39,42–45</sup> (Figures S1 and S2). Thus, it is important to consider absorption edges, EQEs, and  $V_{\text{oc}}$  losses to pick up the most suitable organic material, comprehensively. As shown in Figure 1C, for the case of Y6-based rear cell with ~1.41 eV  $E_{\text{g}}$  (Figure S2B), the  $\text{EQE}_{\text{loss,T}}$  does affect the selection of the front cell materials. The optimal  $E_{\text{g}}$  of the front cell is about 1.95 eV assuming no  $\text{EQE}_{\text{loss,Tmax}}$ , the maximum  $\text{EQE}_{\text{loss,T}}$ , and it gradually changes to 1.7 eV as  $\text{EQE}_{\text{loss,Tmax}}$  increases to 50%, while the corresponding efficiency limit only slightly decreases from 31% to 29% (Figure 1C). Although the 1.95 eV PSC is theoretically more compatible to the Y6-based rear cell, practically the most suitable  $E_{\text{g}}$  is about 1.75 eV, if considering the realistic performance levels of different wide-band-gap perovskites (Figure S3). Taking both model analysis and practical technology status into consideration, we selected the PBDBT-2F:Y6:PC<sub>71</sub>BM system with a  $E_{\text{g}}$  of 1.41 eV as the rear cell and FA<sub>0.8</sub>MA<sub>0.02</sub>Cs<sub>0.18</sub>PbI<sub>1.8</sub>Br<sub>1.2</sub> of 1.77 eV band gap as the absorber of the front cell, whose absorption spectra are depicted in Figure S4.

### Performance Optimizations of the Front and Rear Single-Junction Devices

As shown in Figure 2A, we fabricated the wide-band-gap single-junction PSCs adopting the “p-i-n” structure consisting of Glass/ITO/NiO<sub>x</sub>/FA<sub>0.8</sub>MA<sub>0.02</sub>Cs<sub>0.18</sub>PbI<sub>1.8</sub>Br<sub>1.2</sub>/C<sub>60</sub>/Bathocuproine (BCP)/Ag, while the narrow-band-gap OSCs with the structure of glass/Indium-tin-oxide (ITO)/NiO<sub>x</sub>/PBDBT-2F:Y6:PC<sub>71</sub>BM/C<sub>60</sub>/1,3,5-Tris(1-phenyl-1H-benzimidazol-2-yl)benzene (TPBi)/Ag. Figure 2B shows the schematic of film preparation processes for PSCs and OPVs. It was noteworthy that the gas-pumping method was used to prepare the perovskite films, which improved the device reproducibility compared with the widely applied antisolvent-washing methods.<sup>46,47</sup> For the rear cells, the organic films were fabricated by traditional spin-casting method.

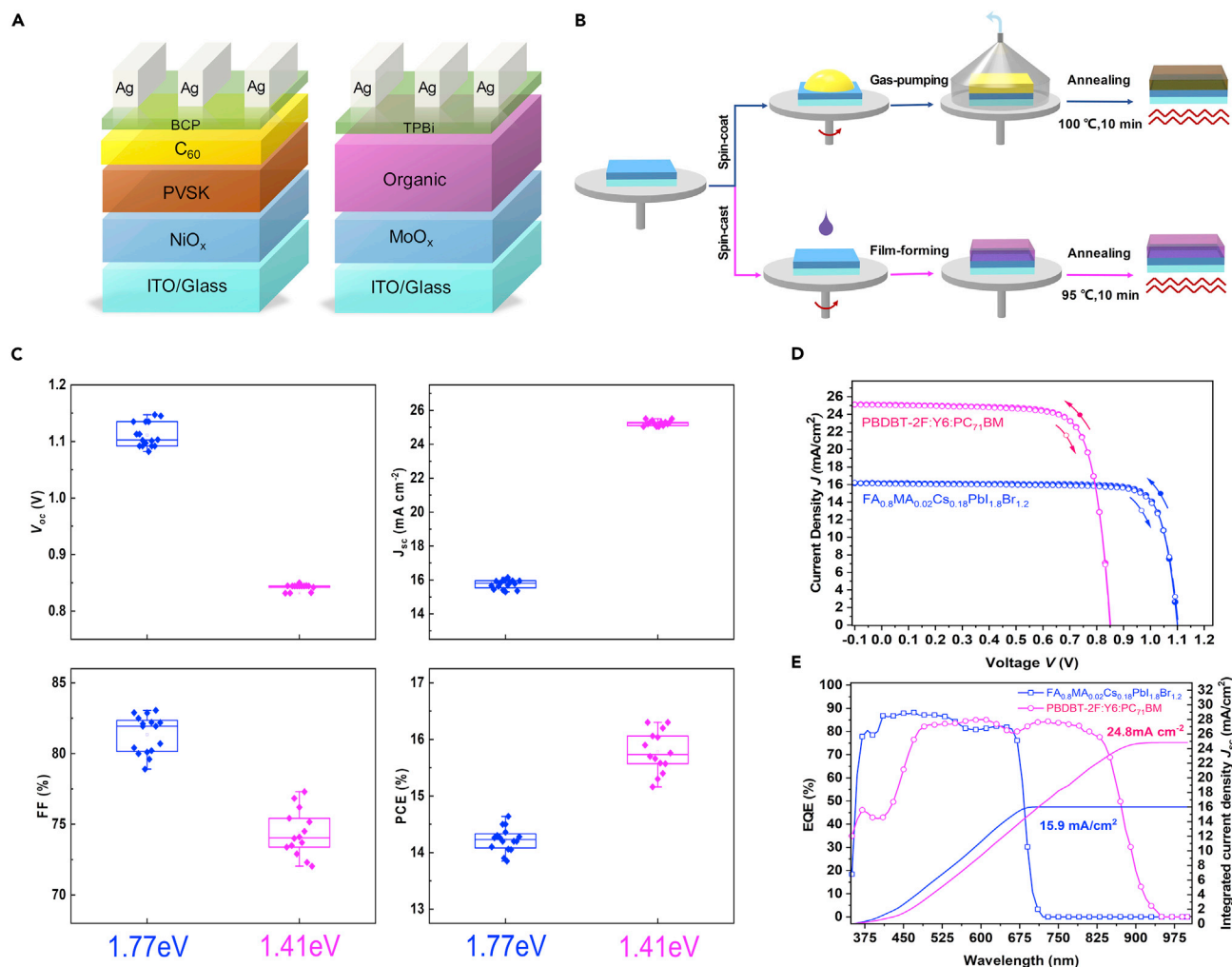


**Figure 2. Device Structures, Preparation Methods, and Device Performances of the  $\text{FA}_{0.8}\text{MA}_{0.02}\text{Cs}_{0.18}\text{PbI}_{1.8}\text{Br}_{1.2}$  and  $\text{PBDBT-2F:Y6:PC}_{71}\text{BM}$  (1:1.2:0.2) Single-Junction Solar Cells**

- (A) Schematics of the Perovskite and Organic Cells.  
 (B) Fabrication processes.  
 (C) Statistics of  $V_{oc}$ ,  $J_{sc}$ ,  $FF$  and  $PCE$  for 16 perovskite front cells and 14 organic rear cells.  
 (D) J-V curves of the champion devices.  
 (E) Corresponding EQE spectra.

Different types of  $\text{NiO}_x$  as hole-transport layers (HTLs) have been studied for the wide-band-gap PSCs. The first one is based on the precursor sol-gel method,<sup>48</sup> denoted as A- $\text{NiO}_x$ . The second one is pre-synthesized  $\text{NiO}_x$  nanoparticles dispersed in deionized water ( $20 \text{ mg mL}^{-1}$ ),<sup>49</sup> denoted as B- $\text{NiO}_x$ . Deposition of B- $\text{NiO}_x$  film on top of A- $\text{NiO}_x$  film forms a stacked HTL, which was denoted as A/B- $\text{NiO}_x$ . The corresponding devices based on the three different HTLs were labeled as device A, B, and C, respectively. The perovskite films grown on different  $\text{NiO}_x$  HTLs showed similar average grain sizes of 90–100 nm (Figures S5C–S5E), while the corresponding surface roughness of the perovskite films varied slightly from 8 to 13 nm, as shown in the Figures S5F–S5H. We carried out ultraviolet photoelectron spectroscopy (UPS) measurements to determine the energy levels of perovskite films ( $\text{FA}_{0.8}\text{MA}_{0.02}\text{Cs}_{0.18}\text{PbI}_{1.8}\text{Br}_{1.2}$ ), A- $\text{NiO}_x$  film, and B- $\text{NiO}_x$  film. It is found that the VBM of B- $\text{NiO}_x$  film is -5.08 eV, which is about 0.14 eV lower than that of A- $\text{NiO}_x$  film,

leading to a more favorable energy alignment with perovskite film with a VBM of -5.58 eV. The stacked NiO<sub>x</sub> film is supposed to form a gradient band alignment and likely to improve the hole-transport efficiency. We further conducted the steady-state photoluminescence (PL) and time-resolved photoluminescence (TRPL) of perovskite films deposited on bare glass, A-NiO<sub>x</sub> film, B-NiO<sub>x</sub> film, and A/B-NiO<sub>x</sub> film to investigate the effect of hole extraction. It should be noted that both interface trap states and charge extractions will alter the PL intensity and lifetime when perovskites are interfaced with different HTLs, but given the same  $V_{oc}$  losses of different devices, we believe the changes of static and dynamic PL signals are mainly determined by different charge extraction efficiencies at interfaces. Observable PL quenching can be found for all cases when comparing the perovskite film on bare glass and perovskite films grown on different types of NiO<sub>x</sub>. It is clear that the strongest PL quenching occurs for the perovskite deposited on the A/B-NiO<sub>x</sub> film, which is also possibly ascribed to the formed gradient band alignment. The charge carrier lifetimes shown in Figure S6D are also consistent with the observation of PL quenching, indicating that the hole extraction when perovskite interfaced with A/B-NiO<sub>x</sub> film is the most efficient. Both the PL and TRPL results support the energy alignment schematic in Figure S6E. The J-V curves of devices based on different NiO<sub>x</sub> HTLs are shown in Figure S6 with the device using the A/B-NiO<sub>x</sub> film exhibiting the highest PCE of 14.7%, based on A-NiO<sub>x</sub> film and B-NiO<sub>x</sub> film. The corresponding EQEs are displayed in Figure S6. To further understand the difference of the loss mechanism, we applied the modified detailed balance model to deduce different loss parameters of the devices.<sup>20,21,50</sup> As shown in the Figure S7, the similar non-radiative rate  $\gamma$  of all three devices was consistent with the similar grain sizes from scanning electron microscope (SEM) images and similar  $V_{oc}$  loss of 0.67 eV. It also confirms that the quenched PL intensity and reduced decay constant of the perovskite at A/B-NiO<sub>x</sub> film are not originating from increased interface defect states but the improved hole extractions.

For the OPV rear subcell, we optimized the device performance by introduction of a small amount of PC<sub>71</sub>BM into the PBDBT-2F:Y6 binary system to form a ternary composite. The corresponding molecular structures and normalized absorption spectra of PBDBT-2F, Y6 and PC<sub>71</sub>BM were presented in Figures S8A and S8B. As shown in Figures S8C and S8D, it was found that the device based on the ternary system: PBDBT-2F:Y6:PC<sub>71</sub>BM with the ratio of 1:1.2:0.2 delivered the highest PCE with increased short-circuit  $J_{sc}$ , mainly owing to a more balanced electron and hole transport.<sup>39</sup> Figures 2C–2E depict the performance of optimized wide-band-gap FA<sub>0.8</sub>MA<sub>0.02</sub>Cs<sub>0.18</sub>Pb<sub>2.8</sub>Br<sub>1.2</sub> PSCs and small-band-gap PBDBT-2F:Y6:PC<sub>71</sub>BM ternary OPVs. Figure 2C presents the statistics of  $V_{oc}$ ,  $J_{sc}$ ,  $FF$  and PCE among 16 perovskite-based cells and 14 organic-based cells. The best FA<sub>0.8</sub>MA<sub>0.02</sub>Cs<sub>0.18</sub>Pb<sub>1.8</sub>Br<sub>1.2</sub> front subcell showed an excellent  $FF$  of 83.1%, a short-circuit current density  $J_{sc}$  of 16.1 mA cm<sup>-2</sup>, and an open-circuit voltage  $V_{oc}$  of 1.10 V, resulting in an efficiency of 14.7%. Whereas, the best ternary OPVs exhibited a  $J_{sc}$  of 25.1 mA cm<sup>-2</sup>, 77.0%  $FF$  and  $V_{oc}$  of 0.842 V, yielding a 16.3% PCE. There were no obvious hysteresis effects for both subcells (Figure 2D; Table 1). As shown in Figure 2E, EQE spectrum of the front cell ended up at 700 nm and produced a current density of 15.9 mA cm<sup>-2</sup>. The narrow band-gap rear cell had a near-plateau EQE spectrum at around 80% from 475 nm to 850 nm, giving a current density of 24.8 mA cm<sup>-2</sup>.

### Optimizing the ICLs and Matching the Currents of Subcells

Monolithically integrated subcells are like two photo-current sources operating in series. Current matching and high-quality ICLs are keys to the tandem performance. Figure 3A shows the ICL design of BCP, Ag nanoparticles, and MoO<sub>x</sub>. Here, the ultra-thin Ag layer acts as a recombination center. Figure 3B shows the absorbed energy

**Table 1. The Device Parameters of the Front and Rear Subcells**

Cells	Scan Direction	$J_{sc}$ ( $\text{mA cm}^{-2}$ )	$V_{oc}$ (V)	FF (%)	PCE (%)
FA <sub>0.8</sub> MA <sub>0.02</sub> CS <sub>0.18</sub> PbI <sub>1.8</sub> Br <sub>1.2</sub>	Reverse	16.1	1.100	83.1	14.7
	Forward	16.1	1.103	81.6	14.5
PBDBT-2F:Y6:PC <sub>71</sub> BM (1:1.2:0.2)	Reverse	25.1	0.842	77.0	16.3
	Forward	25.0	0.842	77.3	16.3

distribution simulated by transfer matrix method.<sup>51</sup> The optical constants of wide band-gap perovskite and small band-gap organic absorbers are shown in [Figure S10](#). The front cell mainly utilizes the visible photons from 350 to 700 nm, while the rear cell absorbs the NIR photons from 700 to 900 nm. Obviously, there was an overlap area between 525 and 675 nm. Benefiting from the very thin ICL and the small absorption extinctions of BCP and MoO<sub>x</sub>, the optical loss of the ICL, including both parasitic absorption and NIR photon (700–900nm) reflection, was approaching zero ([Figure S11](#)). The energy-level schematic is shown in the [Figure 3C](#). Indeed, when there was no super-thin silver inside the ICL, the ohmic contact between the subcells became worse, leading to the J-V curve kinks as shown in [Figure S12A](#). This agrees with the results from other works.<sup>7,28</sup> Ag nanoparticles help lessen the electrical loss, by promoting balanced and efficient carrier recombination. As for the hole transporting layer in ICL, we found at least a 35 nm MoO<sub>x</sub> layer was needed to prevent chloroform from destroying C<sub>60</sub> or BCP ([Figure S12B](#)). As a result, the total thickness of the ICL was only ~40 nm, which is significantly lower than the normal all-perovskite or all-organic tandem cells. To match the current effectively, we established the relationship between the photo-current and the thickness of each subcell, referring to the tandem configuration shown in [Figure 3D](#). The blue curve is highlighted, indicating that the current is matched theoretically. Nearly lying on this curve, a shadow square region is marked, representing that the thicknesses of the FA<sub>0.8</sub>MA<sub>0.02</sub>CS<sub>0.18</sub>PbI<sub>1.8</sub>Br<sub>1.2</sub> front cell (230 ± 10 nm) and PBDBT-2F:Y6:PC<sub>71</sub>BM rear cell (135 ± 5 nm) are employed in this study.

### Perovskite/Organic Monolithic Tandem Performance

Finally, we fabricated monolithic perovskite/organic tandem devices, employing a 1.77 eV wide band-gap FA<sub>0.8</sub>MA<sub>0.02</sub>CS<sub>0.18</sub>PbI<sub>1.8</sub>Br<sub>1.2</sub> (~230 nm) perovskite as front subcell and a 1.41 eV narrow band-gap organic (~135 nm) as rear subcell with the configuration of glass/ITO (~150 nm)/NiO<sub>x</sub> (~60 nm)/wide-band-gap perovskite /C<sub>60</sub> (~20 nm)/BCP (~5 nm)/Ag nanoparticle (~1 nm)/MoO<sub>x</sub> (~35 nm)/low-band-gap OPV/TPBi (~3 nm)/Ag (~80 nm) shown in [Figure 3A](#) and device cross-section SEM image in [Figure 4A](#). In our case, we did solution (NiO<sub>x</sub>, Perovskite)/evaporation (C<sub>60</sub>, BCP, Ag, MoO<sub>x</sub>)/solution (Organic)/evaporation (TPBi, Ag), two alternations to get the ultimate tandem devices. Although the processing is relatively facile compared with the normal perovskite-perovskite tandems, we should further reduce the alternations of solution and non-solution processing to be more manufacturing friendly. The reduction could be realized either by developing a thermally evaporated NIR OPV system or using a fully solution processed ICLs. [Figures 4B](#) and [4C](#) present the J-V and EQE curves of champion tandem cells with corresponding performance parameters summarized in [Table 2](#). The best device shows a notable PCE of 20.6% under reverse scan with  $V_{oc}$  of 1.902 V,  $J_{sc}$  of 13.05 mA cm<sup>-2</sup> and a quite high FF of 83.1%. The  $V_{oc}$  of tandem device is approximately close to the summed photovoltage of the front and back subcells. And it is obvious that the PCE of the champion TSC is clearly much higher than that of each separate subcell, demonstrating the advantage of monolithic tandem configuration. The integrated  $J_{sc}$

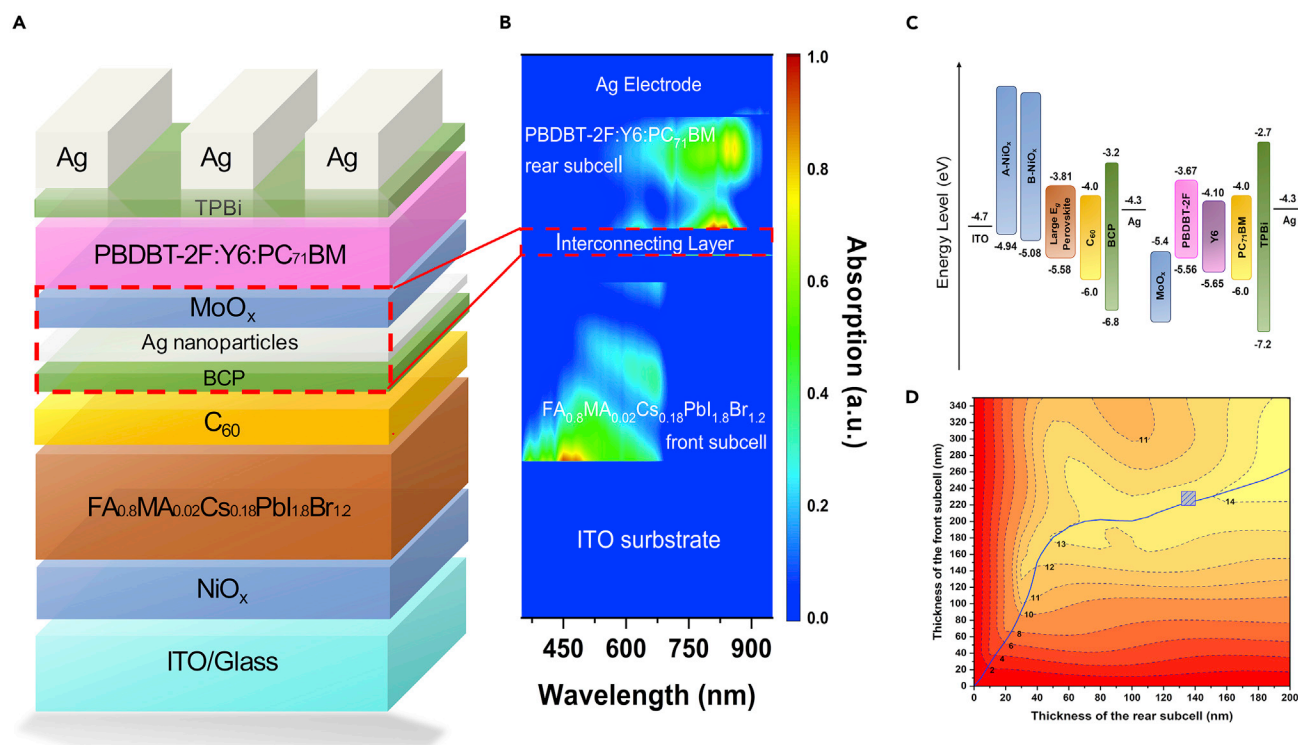


**Figure 3. Design of Perovskite-Organic Tandem Device, Optical Simulation, and Current Matching of Subcells**

- (A) Tandem cell structure with a highlight on ICL design.  
 (B) The distributions of photon absorptions in tandem, simulated by transfer matrix method.  
 (C) Energy-level schematic.  
 (D) Stimulated current density as a function of the variable thicknesses of the front and rear subcells.

values of front and rear subcells from EQE spectra were determined to be exactly the same,  $13.1 \text{ mA cm}^{-2}$ , matching well with  $J_{sc}$  obtained from the J-V measurement. The comparison between absorption and EQE spectra of tandem devices is shown in Figure S13. We also sent our device to the third party institute *SIMIT* (Shanghai, China) for certification, which gave a PCE of 19.54%, slightly lower than that of our in-house measurement (Figure S14). This small PCE drop is possibly due to the slight difference of the solar spectra, especially at the wavelength from 750 nm to 900 nm, resulting in inconsistent current matching (Figure S15). We obtained the stabilized efficiency of 20.6% by tracking the maximum power point (MPP) of the tandem device (Figure 4D) for 20 min, which was consistent with the PCE obtained from J-V scans. Figure 4E shows the histogram of PCE values of 29 tandem devices from three batches. The PCEs distribute compactly between 20% and 20.6%, indicating an impressively high reproducibility of those perovskite/organic tandem devices, which we believe primarily owes to the orthogonal solvents for processing perovskite, organic subcells, as well as the facile ICLs. Figure S16 shows the discrepancy between experimental result and practical efficiency limit. The crucial difference of PCE mainly originates from the significant  $V_{oc}$  losses in both perovskite and organic single-junction devices, indicating that there are significant non-radiative recombination losses in each subcells, while the losses of the ICL is trivial.

Recent results started showing very promising long-term photostability for OPVs,<sup>52,53</sup> but it still suffers from burn-in photodegradation at the initial stage of fatigue.<sup>54,55</sup> As shown in the Figure 4F, OPV rear cells exhibited rapid degradation

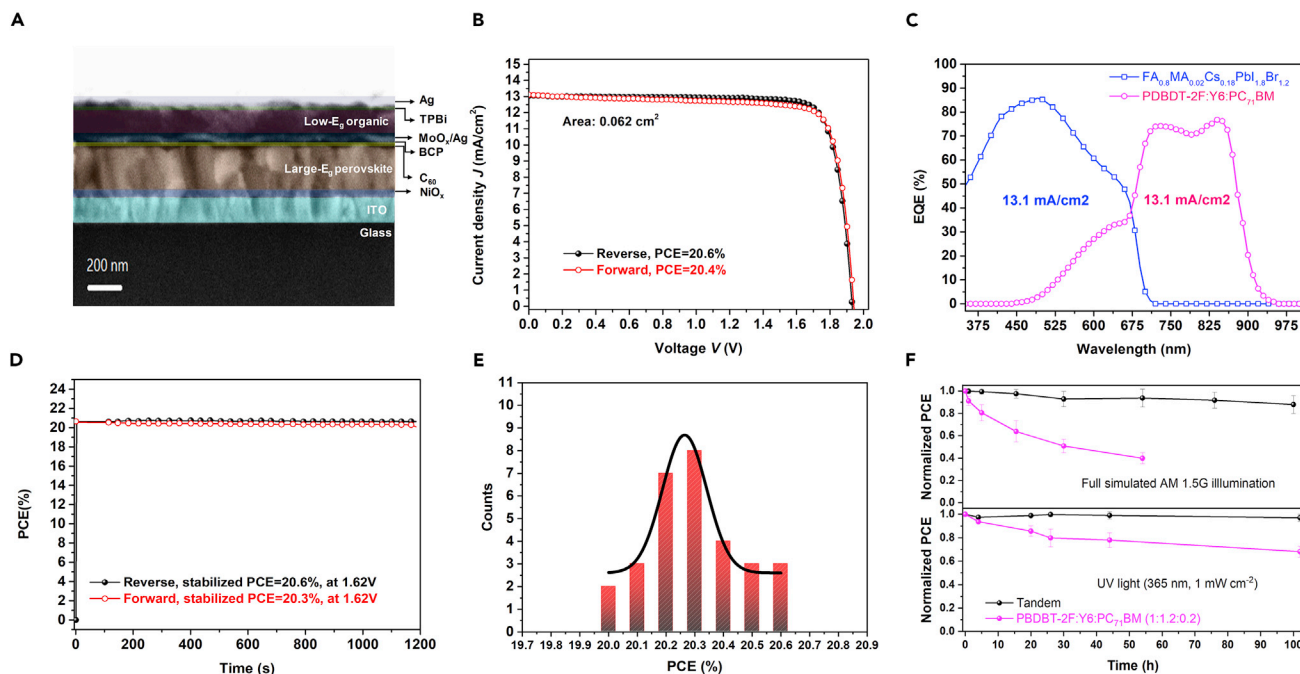


**Figure 4. Device Performance for the 0.062 cm<sup>2</sup> Perovskite-Organic Tandem Cells**

(A) Cross-section SEM.

(B) J-V curves of the champion device with different scan directions.

(C) Corresponding EQE spectrum.

(D) Corresponding MPP tracking in a glovebox under solar simulator.

(E) PCE distributions of 29 devices over three batches. Refer to the Table S2 for detailed parameters of these tandem cells.

(F) Photostability and UV sensitivity tests of tandem cells and OPV subcells. 17 OPVs and 21 tandems were tested under full simulated AM 1.5 G illumination; 16 OPVs and 13 tandems were tested for UV-stability. The devices were stressed under open-circuit conditions. The solar and UV lamps were always on during the fatigue tests, the devices were measured at each testing points as indicated in the Figure 4F and put back to the illuminations without delays. All devices were tested without intentional cooling, such that the actual temperatures of the devices were significantly higher than room temperature.

under one-sun irradiation, retaining only an average ~40% of their initial PCEs after 54 h continuous light soaking. Inspiringly, these TSCs averagely retained more than 88% of their initial PCEs after 100 h continuous light soaking, showing significantly reduced burn-in effect. It should be noted that these tandems have been stored in a N<sub>2</sub>-filled glove box for ~130 days before the 100 h light soaking and remained 95% of their initial PCEs averagely (Figure S17). The OPV device is also known to be very sensitive to UV-light that can trigger photochemical reaction and break organic bonds. In this tandem structure, the perovskite front cell spontaneously serves as the UV filter for the OPV rear cell, such that only an average 3% drop of PCE was observed after 100 h aging under continuous 365nm UV-light (1 mW cm<sup>-2</sup>) illumination. In contrast, OPV single cells only kept ~68% of their initial PCEs.

## Conclusion

In summary, we demonstrated a successful monolithic perovskite/organic TSC with a landmark PCE of 20.6% (certified as 19.54%). Such tandem structure has unique advantages compared with all-perovskite or all-organic TSCs. Orthogonal solvents are used for processing front and rear subcells, which lead to a simplified ICL with negligible optical loss and high reproducibility. Such structure also demonstrates merits on stabilities, the common UV destructive effect of OPVs was significantly reduced

**Table 2. Performance Parameters of the Front Cell, Rear Cell and the Champion 2T Tandem Device**

Cells	Scan Direction	$J_{sc}$ (mA cm <sup>-2</sup> )	$V_{oc}$ (V)	FF (%)	PCE (%)
FA <sub>0.8</sub> MA <sub>0.02</sub> Cs <sub>0.18</sub> PbI <sub>1.8</sub> Br <sub>1.2</sub>	Reverse	15.4	1.113	82.4	14.1
	Forward	15.3	1.135	80.6	14.0
PBDBT-2F:Y6:PC <sub>71</sub> BM (1:1.2:0.2)	Reverse	25.2	0.832	75.2	15.8
	Forward	25.0	0.832	74.8	15.6
2T Tandem Cell (0.062 cm <sup>2</sup> )	Reverse	13.05	1.902	83.1	20.6
	Forward	13.13	1.902	81.5	20.4

with the filtering effect of perovskite layer. Based on the semi-empirical device model developed in this study, we predict a practical efficiency over 30% is approachable as the rapid developing of low-band-gap organic semiconductors and wide-band-gap perovskite materials.

## EXPERIMENTAL PROCEDURES

### Resource Availability

#### Lead Contact

Further information and requests for resources and materials should be directed to and will be fulfilled by the Lead Contact, Yang (Michael) Yang ([yangyang15@zju.edu.cn](mailto:yangyang15@zju.edu.cn)).

#### Materials Availability

The hole-transport layer, NiO<sub>x</sub>, was synthesized by two different methods.<sup>48,49</sup> Other chemicals were commercially available: PC<sub>71</sub>BM (Sigma-Aldrich), PbBr<sub>2</sub>, MAI, FAI, CsI, C<sub>60</sub>, and TPBi (Xi'an Polymer Light Technology), PbI<sub>2</sub> and GuaSCN (Tokyo Chemical Industry Co), PBDBT-2F and Y6 (Solarmer Materials), N,N-Dimethyl formamide (DMF) and Dimethyl sulfoxide (DMSO) (anhydrous, Sigma-Aldrich), chloroform (HPLC, damas-beta).

#### Data and Code Availability

All data are present in the paper and supplementary materials. Other data are available from the lead contact or corresponding author.

### Preparation of NiO<sub>x</sub> Precursor Solution

Herein, the noted A-NiO<sub>x</sub> HTL was prepared by dissolving 0.1244 g of Nicke(II) acetylacetonate in 5 mL ethanol with the addition of 50 μL HCl (38 wt %). The solution was then stirred at room temperature overnight.<sup>48</sup> The other noted B-NiO<sub>x</sub> HTL was prepared by dissolving the NiO<sub>x</sub> nanoparticle solution in deionized water (20 mg mL<sup>-1</sup>). Details on the synthesis procedure of the NiO<sub>x</sub> NP is described elsewhere.<sup>49</sup>

### FA<sub>0.8</sub>MA<sub>0.02</sub>Cs<sub>0.18</sub>PbI<sub>1.8</sub>Br<sub>1.2</sub> Precursor Solution

The precursor solution was prepared by dissolving 0.3165 g of FAI, 0.1066 g of CsI, 0.0071 g of MAI, 0.4242 g of PbI<sub>2</sub>, 0.5066 g of PbBr<sub>2</sub> and 0.0028 g of GuaSCN in 2.3 mL mixed solvents of DMF and DMSO (v/v = 9:1). The solution was stirred on a 70°C hot plate overnight before use. Low dose MA additive was proved to improve the defect tolerance of wide band-gap perovskites.<sup>56</sup> Figure S17 showed almost identical X-ray diffraction patterns for the control film and the perovskite film with GuaSCN additives, indicating that the GuaSCN is not likely to be incorporated into the perovskite lattice, which also agrees with a previous report.<sup>5</sup>

### PBDBT-2F:Y6:PC71BM (1:1.2:0.2) Precursor Solution

The organic solution was prepared by dissolving 0.0080 g of PBDBT-2F, 0.0096 g of Y6 and 0.0016 g of PC<sub>71</sub>BM in 1 mL chloroform. Before use, the solution was stirred at room temperature overnight.

### FA<sub>0.8</sub>MA<sub>0.02</sub>Cs<sub>0.18</sub>PbI<sub>1.8</sub>Br<sub>1.2</sub> Device Fabrication

The ITO-coated substrates (sheet resistance  $\approx 15 \Omega \text{ sq}^{-1}$ ) were cleaned in diluted detergent, deionized water, acetone and isopropanol for 10 min, sequentially, and then UV-ozone treated for 15 min. A-NiO<sub>x</sub> films were coated on the cleaned ITO substrates at 5000 rpm for 30 s and then baked at 300°C under ambient condition for 30 min. After cooling, B-NiO<sub>x</sub> films were coated on them and then dried naturally for 30 min. After that, the substrates were transferred into a N<sub>2</sub>-filled glovebox. After filtering the precursor solution through 0.20- $\mu\text{m}$  PTFE membrane, the FA<sub>0.8</sub>MA<sub>0.02</sub>Cs<sub>0.18</sub>PbI<sub>1.8</sub>Br<sub>1.2</sub> perovskite films were then deposited by spin-coating the precursor solution onto NiO<sub>x</sub> film at 5,000 rpm for 6 s and then transferred to the vacuum chamber as soon as possible for gas-pumping for 6 s. The vacuum level of the vacuum buffer tank was  $-0.1 \text{ MPa}$  when the pumping started. The minor sign of " $-0.1 \text{ MPa}$ " just means that the current vacuum buffer tank is in a vacuum state. The value remains " $-0.1 \text{ MPa}$ " after the 6 s of "gas-pumping." There is a huge volume difference between the tank and vacuum chamber, which results in quite a fast pumping rate. Figure S19 described the schematic setup of the vacuum chamber. The as-prepared films were annealed immediately under 100°C for 10 min. Finally, C<sub>60</sub> ( $\sim 20 \text{ nm}$ ), BCP ( $\sim 5 \text{ nm}$ ) and Ag ( $\sim 80 \text{ nm}$ ) were sequentially deposited by thermal evaporation.

### PBDBT-2F:Y6:PC71BM (1:1.2:0.2) Device Fabrication

The cleaned ITO-coated substrates were UV-ozone treated for 15 min. MoO<sub>x</sub> ( $\sim 35 \text{ nm}$ ) were sequentially evaporated onto the as-prepared substrates with deposition rate of  $0.2 \text{ \AA s}^{-1}$ . After that, the substrates were transferred into a N<sub>2</sub>-filled glovebox. The PBDBT-2F:Y6:PC<sub>71</sub>BM (1:1.2:0.2) organic films were then deposited by spin-casting the organic solution onto MoO<sub>x</sub> film at 3,000 rpm for 60 s. The as-prepared films were annealed immediately under 95°C for 10 min. Finally, TPBi ( $\sim 3 \text{ nm}$ ) and Ag ( $\sim 80 \text{ nm}$ ) were sequentially deposited by thermal evaporation with a deposition rate of  $0.2 \text{ \AA s}^{-1}$  for TPBi and  $0.8 \text{ \AA s}^{-1}$  for Ag.

### Fabrication of Perovskite-Organic 2T Tandem Cell

C<sub>60</sub> ( $\sim 20 \text{ nm}$ )/BCP ( $\sim 5 \text{ nm}$ )/Ag ( $\sim 1 \text{ nm}$ )/MoO<sub>x</sub> ( $\sim 35 \text{ nm}$ ) were sequentially evaporated onto the as-prepared perovskite films with a deposition rate of  $0.2 \text{ \AA s}^{-1}$  for C<sub>60</sub>, BCP and  $0.8 \text{ \AA s}^{-1}$  for Ag, as the ICL. Refer to the organic device fabrication for the follow-up procedures.

### Film and Device Characterization

SEM measurement was obtained on a Hitachi SU8030 electron microscope. Atomic force microscopy (AFM) images were taken on a Cypher S Atomic Force Microscope. The absorption spectrum was carried out by Agilent Carry 7000 UV-Vis spectrometer. UPS was measured by a Thermo Scientific ESCALAB 250 equipment with UVL-Hi high-intensity UV source in an ultrahigh vacuum chamber ( $< 10^{-10} \text{ Torr}$ ). Ellipsometry was carried out by an ellipsometer (M-2000D, J.A. Woollam Co.). Ultima IV diffractometer (Rigaku, graphite monochromatic, Cu K $\alpha$  radiation) detected the perovskite films at room temperature with a scanning rate of  $0.1^\circ \text{ s}^{-1}$  over the Bragg angle range of  $10.0^\circ$ – $65.0^\circ$  ( $2\theta$ ). Steady-state PL and TRPL were detected using a home-setup confocal fluorescence system. The samples were excited with a CW laser at 532nm (for PL measurement) and a picosecond (ps) laser at 515 nm (for TRPL measurement). PL spectra were measured using a spectrograph (Princeton Instruments) with a liquid-N<sub>2</sub>-cooled charge-coupled device

(CCD) (PrLoN). TRPL decay kinetics were collected at room temperature using a time-correlated single photon counting (TCSPC) module (PicoHarp 300) and a scratch pad memory (SPAD) detector (IDQ, id100) with an instrument response function  $\sim 100$  ps. Current density-voltage characteristics (J-V) were detected under AM1.5G light ( $100 \text{ mW cm}^{-2}$ ) using the xenon arc lamp of a Class A solar simulator. Light intensity was calibrated using a Newport-calibrated mono crystalline Si diode. The Keithley 2400 source meter was used for I-V measurement. EQE was carried out with an integrated home-setup system, based on ASTM E2236 standard test methods.<sup>57</sup> EQE spectra of the front and rear subcells inside the TSCs were characterized by additionally applying the bias monochromatic light sources with emission peaks of 850 and 500 nm, respectively.

### Solar Cell Certification

Photovoltaic certification test was conducted by the Test and Calibration Centre of the New Energy Device and Module, *SIMIT* (Shanghai, China). The J-V characteristics were measured by a class AAA super solar simulator with dual lamp (xenon and halogen). The irradiance is set to  $100 \text{ mW cm}^{-2}$  using a silicon reference solar cell calibrated by National Renewable Energy Laboratory (NREL). The spectral mismatch was calculated and corrected according to IEC 60904-7:2008. The EQE of the device was measured by the spectral response measurement system with three grating monochromator. Refer to the [Figure S14](#) for more details.

### SUPPLEMENTAL INFORMATION

Supplemental Information can be found online at <https://doi.org/10.1016/j.joule.2020.06.006>.

### ACKNOWLEDGMENTS

This work is supported by the National Key Research and Development Program of China (2017YFA0207700), National Key Research and Development Program of Zhejiang Province (2018C04SA170313), Outstanding Youth Fund of Zhejiang Natural Science Foundation of China (LR18F050001) and Natural Science Foundation of China (61804134, 61705194).

### AUTHOR CONTRIBUTIONS

Y.(M).Y. conceived the idea and guided the work; W.S. provided guidance for the device modeling; X.C. prepared and characterized single junctions and tandem photovoltaics, and was responsible for the device simulations; Z.J. prepared the OSCs and participated in the efficiency certification; H.Z. and Z.C. mainly undertook PL, AFM, and UPS characterizations. L.B. synthesized HTLs; F.T. was responsible for the photostability test; J.C. built the gas-pumping setup for fabricating PVSCs; X.C. participated in the drawing work; T.L. and X.X. participated in the useful discussions; C.Y. and W.S. assisted on transmission and reflection spectra measurements. The manuscript was mainly written by X.C., T.J., and Y.(M).Y.; all the authors commented on the manuscript.

### DECLARATION OF INTERESTS

Authors declare no competing interests.

Received: March 10, 2020

Revised: April 22, 2020

Accepted: June 3, 2020

Published: July 1, 2020

REFERENCES

- Berry, J.J., van de Lagemaat, J., Al-Jassim, M.M., Kurtz, S., Yan, Y., and Zhu, K. (2017). Perovskite photovoltaics: the path to a printable terawatt-scale technology. *ACS Energy Lett.* *2*, 2540–2544.
- Li, G., Zhu, R., and Yang, Y. (2012). Polymer solar cells. *Nat. Photonics* *6*, 153–161.
- Yang, Y., and Li, G. (2015). *Progress in High-Efficient Solution Process Organic Photovoltaic Devices* (Springer-Verlag Berlin Heidelberg).
- Eperon, G.E., Leijtens, T., Bush, K.A., Prasanna, R., Green, T., Wang, J.T., McMeekin, D.P., Volonakis, G., Milot, R.L., May, R., et al. (2016). Perovskite-perovskite tandem photovoltaics with optimized band gaps. *Science* *354*, 861–865.
- Tong, J., Song, Z., Kim, D.H., Chen, X., Chen, C., Palmstrom, A.F., Ndione, P.F., Reese, M.O., Dunfield, S.P., Reid, O.G., et al. (2019). Carrier lifetimes of >1  $\mu$ s in Sn-Pb perovskites enable efficient all-perovskite tandem solar cells. *Science* *364*, 475–479.
- Rajagopal, A., Yang, Z., Jo, S.B., Braly, I.L., Liang, P.W., Hillhouse, H.W., and Jen, A.K. (2017). Highly efficient perovskite-perovskite tandem solar cells reaching 80% of the theoretical limit in photovoltage. *Adv. Mater.* *29*, 1602121.
- Zhao, D., Chen, C., Wang, C., Junda, M.M., Song, Z., Grice, C.R., Yu, Y., Li, C., Subedi, B., Podraza, N.J., et al. (2018). Efficient two-terminal all-perovskite tandem solar cells enabled by high-quality low-bandgap absorber layers. *Nat. Energy* *3*, 1093–1100.
- Forgács, D., Gil-Escrig, L., Pérez-Del-Rey, D., Mombiona, C., Werner, J., Niesen, B., Ballif, C., Sessolo, M., and Bolink, H.J. (2017). Efficient monolithic perovskite/perovskite tandem solar cells. *Adv. Energy Mater.* *7*, 1602121.
- Palmstrom, A.F., Eperon, G.E., Leijtens, T., Prasanna, R., Habisreutinger, S.N., Nemeth, W., Gaulding, E.A., Dunfield, S.P., Reese, M., Nanayakkara, S., et al. (2019). Enabling flexible all-perovskite tandem solar cells. *Joule* *3*, 2193–2204.
- Lin, R., Xiao, K., Qin, Z., Han, Q., Zhang, C., Wei, M., Saidaminov, M.I., Gao, Y., Xu, J., Xiao, M., et al. (2019). Monolithic all-perovskite tandem solar cells with 24.8% efficiency exploiting comproportionation to suppress Sn(II) oxidation in precursor ink. *Nat. Energy* *4*, 864–873.
- Meng, L., Zhang, Y., Wan, X., Li, C., Zhang, X., Wang, Y., Ke, X., Xiao, Z., Ding, L., Xia, R., et al. (2018). Organic and solution-processed tandem solar cells with 17.3% efficiency. *Science* *361*, 1094–1098.
- Che, X., Li, Y., Qu, Y., and Forrest, S.R. (2018). High fabrication yield organic tandem photovoltaics combining vacuum- and solution-processed subcells with 15% efficiency. *Nat. Energy* *3*, 422–427.
- You, J., Chen, C.C., Hong, Z., Yoshimura, K., Ohya, K., Xu, R., Ye, S., Gao, J., Li, G., and Yang, Y. (2013). 10.2% power conversion efficiency polymer tandem solar cells consisting of two identical sub-cells. *Adv. Mater. Weinh.* *25*, 3973–3978.
- Chang, S.Y., Lin, Y.C., Sun, P.Y., Hsieh, Y.T., Meng, L., Bae, S.H., Su, Y.W., Huang, W.C., Zhu, C.H., Li, G., et al. (2017). High-efficiency organic tandem solar cells With effective transition metal chelates interconnecting layer. *Sol. RRL* *1*, 1700139.
- Zhang, K., Fan, B.B., Xia, R.X., Liu, X., Hu, Z.C., Gu, H.G., Liu, S.Y., Yip, H.L., Ying, L., Huang, F., and Cao, Y. (2018). Highly efficient tandem organic solar cell enabled by environmentally friendly solvent processed polymeric interconnecting layer. *Adv. Energy Mater.* *8*, 1703180.
- Zhang, Y., Kan, B., Sun, Y., Wang, Y., Xia, R., Ke, X., Yi, Y.Q., Li, C., Yip, H.L., Wan, X., et al. (2018). Nonfullerene tandem organic solar cells with high performance of 14.11%. *Adv. Mater.* *30*, e1707508.
- Leijtens, T., Bush, K.A., Prasanna, R., and McGehee, M.D. (2018). Opportunities and challenges for tandem solar cells using metal halide perovskite semiconductors. *Nat. Energy* *3*, 828–838.
- Liu, S., Yuan, J., Deng, W.Y., Luo, M., Xie, Y., Liang, Q.B., Zou, Y.P., He, Z.C., Wu, H.B., and Cao, Y. (2020). High-efficiency organic solar cells with low non-radiative recombination loss and low energetic disorder. *Nat. Photonics* *14*, 300–305.
- Cui, Y., Yao, H., Zhang, J., Zhang, T., Wang, Y., Hong, L., Xian, K., Xu, B., Zhang, S., Peng, J., et al. (2019). Over 16% efficiency organic photovoltaic cells enabled by a chlorinated acceptor with increased open-circuit voltages. *Nat. Commun.* *10*, 2515.
- Jiang, T.M., Chen, Z., Chen, X., Chen, X.Y., Xu, X.H., Liu, T.Y., Bai, L.Z., Yang, D.X., Di, D.W., Sha, W.E.I., et al. (2019). Power conversion efficiency enhancement of low-bandgap mixed Pb-Sn perovskite solar cells by improved interfacial charge transfer. *ACS Energy Lett.* *4*, 1784–1790.
- Jiang, T., Chen, Z., Chen, X., Liu, T., Chen, X., Sha, W.E.I., Zhu, H., and Yang, M.Y. (2019). Realizing high efficiency over 20% of low-bandgap Pb-Sn-alloyed perovskite solar cells by in situ reduction of Sn<sup>4+</sup>. *Sol. RRL* *4*, 1900467.
- Kromdijk, J., Glowacka, K., Leonelli, L., Gabilly, S.T., Iwai, M., Niyogi, K.K., and Long, S.P. (2016). Improving photosynthesis and crop productivity by accelerating recovery from photoprotection. *Science* *354*, 857–861.
- Yang, Z., Yu, Z., Wei, H., Xiao, X., Ni, Z., Chen, B., Deng, Y., Habisreutinger, S.N., Chen, X., Wang, K., et al. (2019). Enhancing electron diffusion length in narrow-bandgap perovskites for efficient monolithic perovskite tandem solar cells. *Nat. Commun.* *10*, 4498.
- Prasanna, R., Leijtens, T., Dunfield, S.P., Raiford, J.A., Wolf, E.J., Swifter, S.A., Werner, J., Eperon, G.E., de Paula, C., Palmstrom, A.F., et al. (2019). Design of low bandgap tin-lead halide perovskite solar cells to achieve thermal, atmospheric and operational stability. *Nat. Energy* *4*, 939–947.
- Zuo, L., Shi, X., Fu, W., and Jen, A.K. (2019). Highly efficient semitransparent solar cells with selective absorption and tandem architecture. *Adv. Mater.* *31*, e1901683.
- Li, Z., Wu, S., Zhang, J., Lee, K.C., Lei, H., Lin, F., Wang, Z., Zhu, Z., and Jen, A.K.Y. (2020). Hybrid perovskite-organic flexible tandem solar cell enabling highly efficient electrocatalysis overall water splitting. *Adv. Energy Mater.* *10*, 2000361.
- Chen, C.-C., Bae, S.-H., Chang, W.-H., Hong, Z., Li, G., Chen, Q., Zhou, H., and Yang, Y. (2015). Perovskite/polymer monolithic hybrid tandem solar cells utilizing a low-temperature, full solution process. *Mater. Horiz.* *2*, 203–211.
- Chen, W., Zhang, J., Xu, G., Xue, R., Li, Y., Zhou, Y., Hou, J., and Li, Y. (2018). A semitransparent inorganic perovskite film for overcoming ultraviolet light instability of organic solar cells and achieving 14.03% efficiency. *Adv. Mater.* *30*, e1800855.
- Liu, J., Lu, S., Zhu, L., Li, X., and Choy, W.C. (2016). Perovskite-organic hybrid tandem solar cells using a nanostructured perovskite layer as the light window and a PFN/doped-MoO<sub>3</sub>/MoO<sub>3</sub> multilayer as the interconnecting layer. *Nanoscale* *8*, 3638–3646.
- Zeng, Q., Liu, L., Xiao, Z., Liu, F., Hua, Y., Yuan, Y., and Ding, L. (2019). A two-terminal all-inorganic perovskite/organic tandem solar cell. *Sci. Bull.* *64*, 885–887.
- Liu, Y., Renna, L.A., Bag, M., Page, Z.A., Kim, P., Choi, J., Emrick, T., Venkataraman, D., and Russell, T.P. (2016). High efficiency tandem thin-perovskite/polymer solar cells with a graded recombination layer. *ACS Appl. Mater. Interfaces* *8*, 7070–7076.
- Wang, Y., Qian, D., Cui, Y., Zhang, H., Hou, J., Vandewal, K., Kirchartz, T., and Gao, F. (2018). Optical gaps of organic solar cells as a reference for comparing voltage losses. *Adv. Energy Mater.* *8*, 1801352.
- Xie, Q., Liao, X., Chen, L., Zhang, M., Gao, K., Huang, B., Xu, H., Liu, F., Jen, A.K.-Y., and Chen, Y. (2019). Random copolymerization realized high efficient polymer solar cells with a record fill factor near 80%. *Nano Energy* *61*, 228–235.
- Zheng, Z., Hu, Q., Zhang, S., Zhang, D., Wang, J., Xie, S., Wang, R., Qin, Y., Li, W., Hong, L., et al. (2018). A highly efficient non-fullerene organic solar cell with a fill factor over 0.80 enabled by a fine-tuned hole-transporting layer. *Adv. Mater.* <https://doi.org/10.1002/adma.201801801>.
- Rosenthal, K.D., Hughes, M.P., Luginbuhl, B.R., Ran, N.A., Karki, A., Ko, S.-J., Hu, H., Wang, M., Ade, H., and Nguyen, T.-Q. (2019). Quantifying and understanding voltage losses due to nonradiative recombination in bulk heterojunction organic solar cells with low energetic offsets. *Adv. Energy Mater.* *9*, 1901077.
- Yuan, J., Huang, T., Cheng, P., Zou, Y., Zhang, H., Yang, J.L., Chang, S.Y., Zhang, Z., Huang, W., Wang, R., et al. (2019). Author correction: enabling low voltage losses and high

- photocurrent in fullerene-free organic photovoltaics. *Nat. Commun.* 10, 1624.
37. Han, Q., Hsieh, Y.T., Meng, L., Wu, J.L., Sun, P., Yao, E.P., Chang, S.Y., Bae, S.H., Kato, T., Bermudez, V., and Yang, Y. (2018). High-performance perovskite/Cu(In,Ga)Se<sub>2</sub> monolithic tandem solar cells. *Science* 361, 904–908.
  38. Park, S.H., Roy, A., Beaupré, S., Cho, S., Coates, N., Moon, J.S., Moses, D., Leclerc, M., Lee, K., and Heeger, A.J. (2009). Bulk heterojunction solar cells with internal quantum efficiency approaching 100%. *Nat. Photonics* 3, 297–302.
  39. Yu, R., Yao, H., Cui, Y., Hong, L., He, C., and Hou, J. (2019). Improved charge transport and reduced nonradiative energy loss enable over 16% efficiency in ternary polymer solar cells. *Adv. Mater.* 31, e1902302.
  40. Xiao, Z., Jia, X., and Ding, L. (2017). Ternary organic solar cells offer 14% power conversion efficiency. *Sci. Bull.* 62, 1562–1564.
  41. Chen, Y., Liu, T., Hu, H., Ma, T., Lai, J.Y.L., Zhang, J., Ade, H., and Yan, H. (2018). Modulation of end groups for low-bandgap nonfullerene acceptors enabling high-performance organic solar cells. *Adv. Energy Mater.* 8, 1801203.
  42. Xu, X., Feng, K., Bi, Z., Ma, W., Zhang, G., and Peng, Q. (2019). Single-junction polymer solar cells with 16.35% efficiency enabled by a platinum (II) complexation strategy. *Adv. Mater.* 31, e1901872.
  43. Yuan, J., Zhang, Y., Zhou, L., Zhang, G., Yip, H.-L., Lau, T.-K., Lu, X., Zhu, C., Peng, H., Johnson, P.A., et al. (2019). Single-junction organic solar cell with over 15% efficiency using fused-ring acceptor with electron-deficient core. *Joule* 3, 1140–1151.
  44. Cui, Y., Yao, H., Zhang, J., Xian, K., Zhang, T., Hong, L., Wang, Y., Xu, Y., Ma, K., An, C., et al. (2020). Single-junction organic photovoltaic cells with approaching 18% efficiency. *Adv. Mater.* 32, 1908205.
  45. Zhu, L., Zhang, M., Zhou, G.Q., Hao, T.Y., Xu, J.Q., Wang, J., Qiu, C.Q., Prine, N., Ali, J., Feng, W., et al. (2020). Efficient organic solar cell with 16.88% efficiency enabled by refined acceptor crystallization and morphology with improved charge transfer and transport properties. *Adv. Energy Mater.* 10, 1904234.
  46. Ding, B., Li, Y., Huang, S.-Y., Chu, Q.-Q., Li, C.-X., Li, C.-J., and Yang, G.-J. (2017). Material nucleation/growth competition tuning towards highly reproducible planar perovskite solar cells with efficiency exceeding 20%. *J. Mater. Chem. A* 5, 6840–6848.
  47. Li, X., Bi, D., Yi, C., Décoppet, J.D., Luo, J., Zakeeruddin, S.M., Hagfeldt, A., and Grätzel, M. (2016). A vacuum flash-assisted solution process for high-efficiency large-area perovskite solar cells. *Science* 353, 58–62.
  48. Zhu, Z., Zhao, D., Chueh, C.-C., Shi, X., Li, Z., and Jen, A.K.-Y. (2018). Highly efficient and stable perovskite solar cells enabled by all-crosslinked charge-transporting layers. *Joule* 2, 168–183.
  49. Lee, K.T., Jang, J.Y., Park, S.J., Ok, S.A., and Park, H.J. (2017). Incident-angle-controlled semitransparent colored perovskite solar cells with improved efficiency exploiting a multilayer dielectric mirror. *Nanoscale* 9, 13983–13989.
  50. Sha, W.E.I., Zhang, H., Wang, Z.S., Zhu, H.L., Ren, X., Lin, F., Jen, A.K.-Y., and Choy, W.C.H. (2018). Quantifying efficiency loss of perovskite solar cells by a modified detailed balance model. *Adv. Energy Mater.* 8, 1701586.
  51. Burkhard, G.F., Hoke, E.T., and McGehee, M.D. (2010). Accounting for interference, scattering, and electrode absorption to make accurate internal quantum efficiency measurements in organic and other thin solar cells. *Adv. Mater.* 22, 3293–3297.
  52. Burlingame, Q., Huang, X., Liu, X., Jeong, C., Coburn, C., and Forrest, S.R. (2019). Intrinsically stable organic solar cells under high-intensity illumination. *Nature* 573, 394–397.
  53. Baran, D., Ashraf, R.S., Hanifi, D.A., Abdelsamie, M., Gasparini, N., Röhr, J.A., Holliday, S., Wadsworth, A., Lockett, S., Neophytou, M., et al. (2017). Reducing the efficiency–stability–cost gap of organic photovoltaics with highly efficient and stable small molecule acceptor ternary solar cells. *Nat. Mater.* 16, 363–369.
  54. Duan, L.P., Yi, H.M., Zhang, Y., Haque, F., Xu, C., and Uddin, A. (2019). Comparative study of light- and thermal-induced degradation for both fullerene and non-fullerene-based organic solar cells. *Sustain. Energy Fuels* 3, 723–735.
  55. Kimura, H., Fukuda, K., Jinno, H., Park, S., Saito, M., Osaka, I., Takimiya, K., Umezū, S., and Someya, T. (2019). High operation stability of ultraflexible organic solar cells with ultraviolet-filtering substrates. *Adv. Mater.* 31, e1808033.
  56. Tan, H., Che, F., Wei, M., Zhao, Y., Saidaminov, M.I., Todorović, P., Broberg, D., Walters, G., Tan, F., Zhuang, T., et al. (2018). Dipolar cations confer defect tolerance in wide-bandgap metal halide perovskites. *Nat. Commun.* 9, 3100.
  57. Timmreck, R., Meyer, T., Gilot, J., Seifert, H., Mueller, T., Furlan, A., Wienk, M.M., Wynands, D., Hohl-Ebinger, J., Warta, W., et al. (2015). Characterization of tandem organic solar cells. *Nat. Photonics* 9, 478–479.